Supplementary Information (SI) for Nanoscale.
This journal is © The Royal Society of Chemistry 2025

Supplementary Electronic Information for:

Magnetoelastic Anisotropy Drives Localized Magnetization Reversal in 3D Nanowire Networks

Laura G. Vivas*,[1] Alejandra Ruiz-Clavijo,[1] Olga Caballero-Calero,[1] David Navas,[2] Amanda A. Ordoñez-Cencerrado,[3] Cristina V. Manzano,[1] Ruy Sanz,[3] and Marisol Martín-González*[1]

[1)] *Instituto de Micro y Nanotecnología, IMN-CNM, CSIC (CEI UAM+CSIC) Isaac Newton, Tres Cantos, Madrid, 8, E-28760 Spain*

[2)] *Instituto de Ciencia de Materiales de Madrid, CSIC, Cantoblanco, 28049 Madrid, Spain*

[3)] *National Institute for Aerospace Technology (INTA), Payloads and Space Science Department, Space Magnetism Area, Torrejón de Ardoz, Madrid, 28850 Spain*

(*Electronic mail: laura.g.vivas@csic.es; Marisol.Martin@csic.es)

(Dated: 19 December 2024)

CONTENTS

SUPPLEMENTARY EXPERIMENTAL RESULTS

S1. Transmission electron backscattered diffraction on Ni nanowires

Figure S1 shows transmission electron backscattered diffraction (t-EBSD) on Ni nanowires. This technique enabled us to map the crystal structure along several Ni nanowires, revealing a polycrystalline structure in good agreement with the XRD results shown in Fig. 1(b) of the main text. Using t-EBSD, we observed that the nanowires are composed of grains approximately 20 nm in size, along with larger grains measuring 100–200 nm in length.

Most grains were approximately 20 nm in size, with some larger grains measuring 100–200 nm. These larger grains exhibited the same crystal orientation but displayed a 60° rotation angle around the (111) plane of the FCC crystal structure (from purple to magenta), forming Σ3 twin boundaries with threefold symmetry and a mirrored lattice structure across the boundaries. These types of boundaries are known to enhance the mechanical properties of materials, such as strength and ductility, by impeding the movement of dislocations.[1]

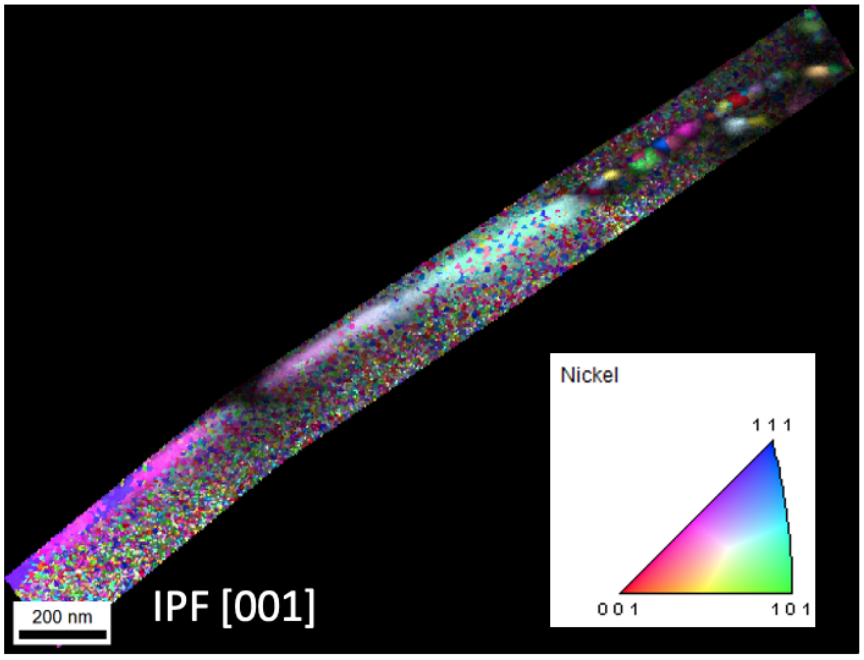

FIG. S1. Transmission electron backscattered diffraction t-EBSD Inverse pole figures (IPF) maps in [001]. The color code for the maps is given in the stereographic triangle. The orientation of the nickel unit cells is indicated by the color code.

SUPPLEMENTARY COMPUTATIONAL RESULTS

S2. Hysteresis loops using standard micromagnetic parameters for nickel

We conducted micromagnetic simulations of hysteresis loops using bulk micromagnetic values in the absence of magnetoelastic anisotropy. Figure S2 (a) shows the experimental results, while Figure S2 (b) presents the corresponding micromagnetic simulation outcomes. The reversal processes for both the in-plane (IP) and out-of-plane (OOP) configurations are illustrated in Figs. S3 and S4, respectively. These reversals occur through delocalized intermediate states that extend throughout the nanowires.

For the IP configuration, as the magnetic field decreases, the shape anisotropy causes the magnetization to align along the nanowire axis (along the z-component). Due to dipolar interactions between adjacent nanowires, their magnetizations tend to align in an antiparallel manner. In contrast, for the OOP configuration, the $y-$component of the magnetization exhibits states that extend across the nanowires, with the reversal proceeding in a wire-by-wire fashion, as anticipated.

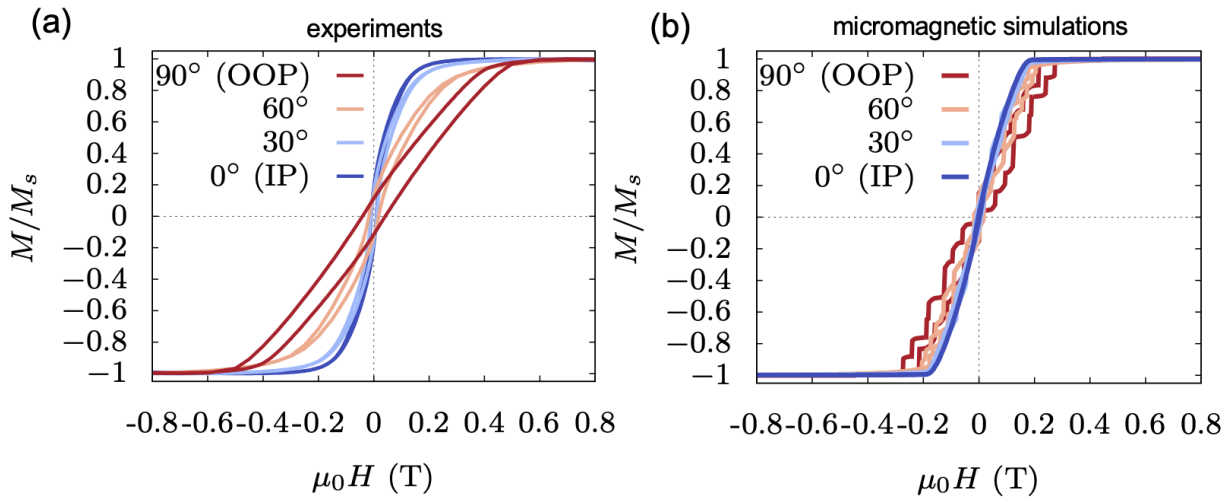

FIG. S2. Angle-dependent hysteresis loops. (a) Experimental data and (b) micromagnetic simulations.

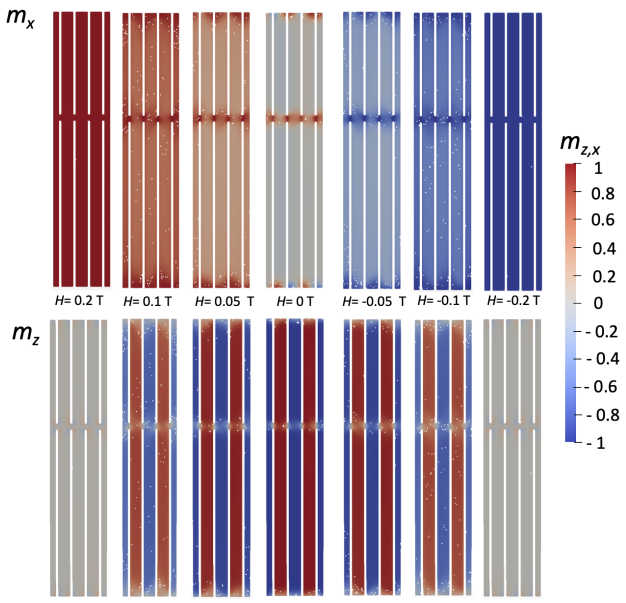

FIG. S3. Magnetic configurations during reversal for the IP configuration of a slice of the central nanowires in our micromagnetic model at various magnetic field strengths near remanence. (Top panel) Micromagnetic configurations of the m_x component. (Bottom panel) Micromagnetic configurations of the m_z component.

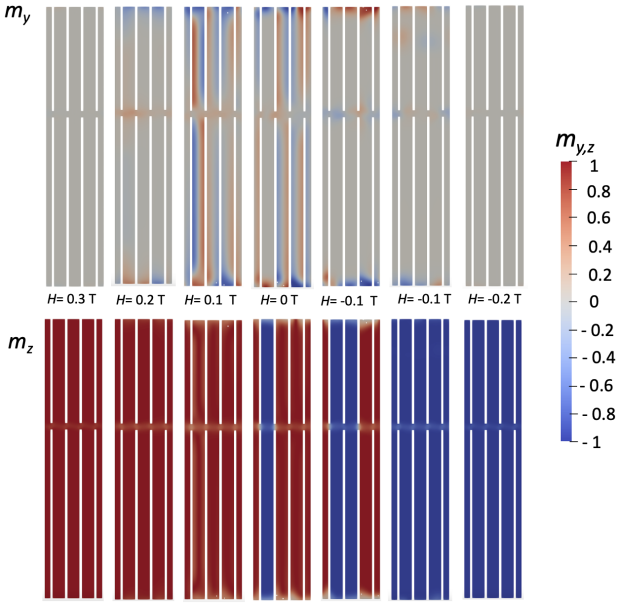

FIG. S4. Magnetic configurations during reversal for the OOP configuration of a slice of the central nanowires in our micromagnetic model at various magnetic field strengths around remanence. (Top panel) Micromagnetic configurations of the m_y component. (Bottom panel) Micromagnetic configurations of the m_z component.

S3. Hysteresis loops as a function of the magneto-elastic anisotropy value

We have conducted simulations of hysteresis loops for a range of magnetoelastic anisotropy values, K_{me}, for the in-plane anisotropy axis. Specifically, for each nanograin composing the components of the 3DNNs, we assume that the anisotropy axis direction follows a quasi-random orientation, represented by the vector $\mathbf{u}_{me} = (1 * \mathrm{ran}(), 1 * \mathrm{ran}(), 0)$. Here, ran() is a random number ranging from -1 to 1.

Figure S5(a) shows the results for values ranging from $K_{\mathrm{me}} = 5 \times 10^3$ J/m^3 to $K_{\mathrm{me}} = 1 \times 10^5$ J/m^3. Black symbols corresponds to the experimental values described in the main text.

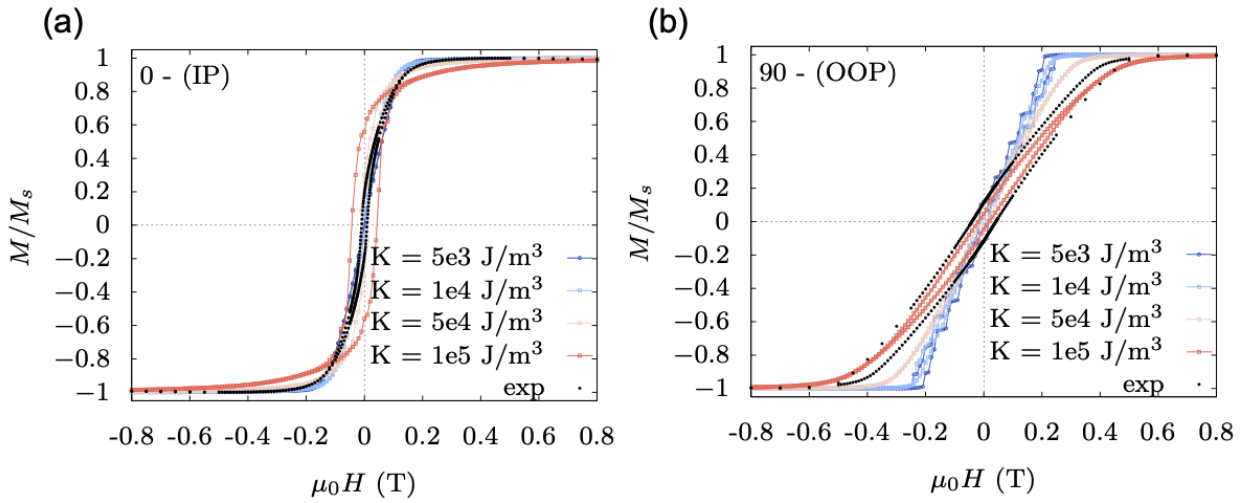

FIG. S5. Hysteresis loops calculated via micromagnetic simulations for a range of magnetoelastic anisotropy values, $K = K_{\mathrm{me}}$. Black symbols corresponds to the experimental values described in the main text. (a) In-plane (IP) configuration. (b) Out-of-plane (OOP) configuration.

S4. Hysteresis loops as a function of the magneto-elastic anisotropy axis direction

We have conducted simulations of hysteresis loops for a range of directions for the in-plane anisotropy axis. Specifically, for each nanograin composing the components of the 3DNNs, we assume that the anisotropy axis direction follows a quasi-random orientation, represented by the vector $\mathbf{u}_{me} = (1 * \text{ran}(), 1 * \text{ran}(), z)$, with $z = 0, 1/2, 1, 5$. Here, ran() is a random number ranging from -1 to 1.

Figures S6(a) and (b) shows the results for the OOP and IP configurations, respectively. It can be observed that the OOP configuration is less susceptible than the IP configuration to variations in the anisotropy axis direction distribution.

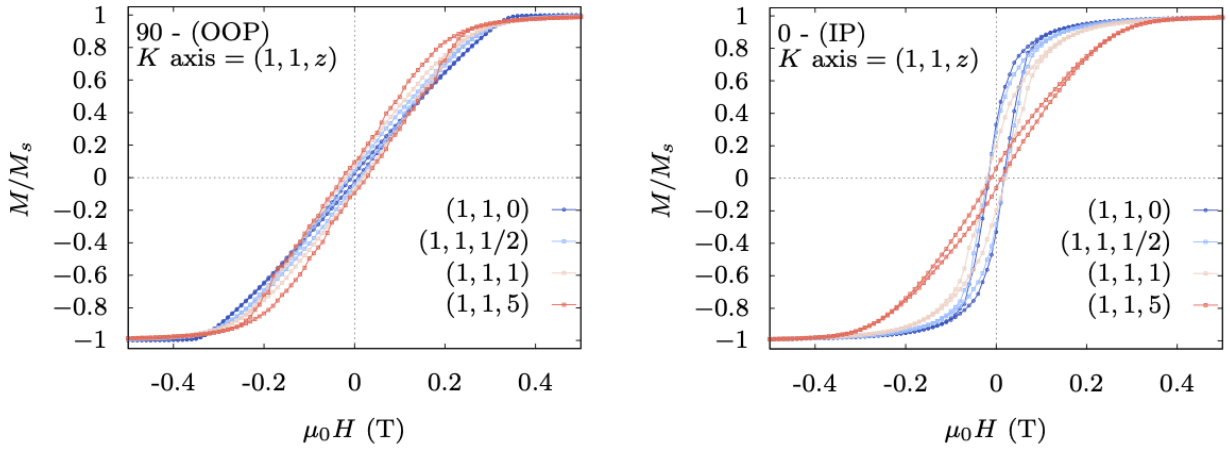

FIG. S6. Hysteresis loops calculated via micromagnetic simulations for a range of magnetoelastic anisotropy direction distribution, $\mathbf{u}_{me} = (1 * \text{ran}(), 1 * \text{ran}(), z)$, with $z = 0, 1/2, 1, 5$. (a) In-plane (IP) configuration. (b) Out-of-plane (OOP) configuration.

S5. Hysteresis loops using standard micromagnetic parameters for nickel+zero exchange between grains

We conducted micromagnetic simulations of the hysteresis loops using bulk micromagnetic values in the absence of both magnetoelastic anisotropy and exchange interaction between computational grains. We demonstrate that localization of magnetization reversal is not realized by just neglecting the exchange between computational grains.

Figure S7 (a) shows the experimental results, while Figure S7 (b) presents the corresponding micromagnetic simulation outcomes. The reversal processes for both the in-plane (IP) and out-of-plane (OOP) configurations are illustrated in Figs. S8 and S9, respectively. These reversals occur through delocalized intermediate states that extend throughout the nanowires.

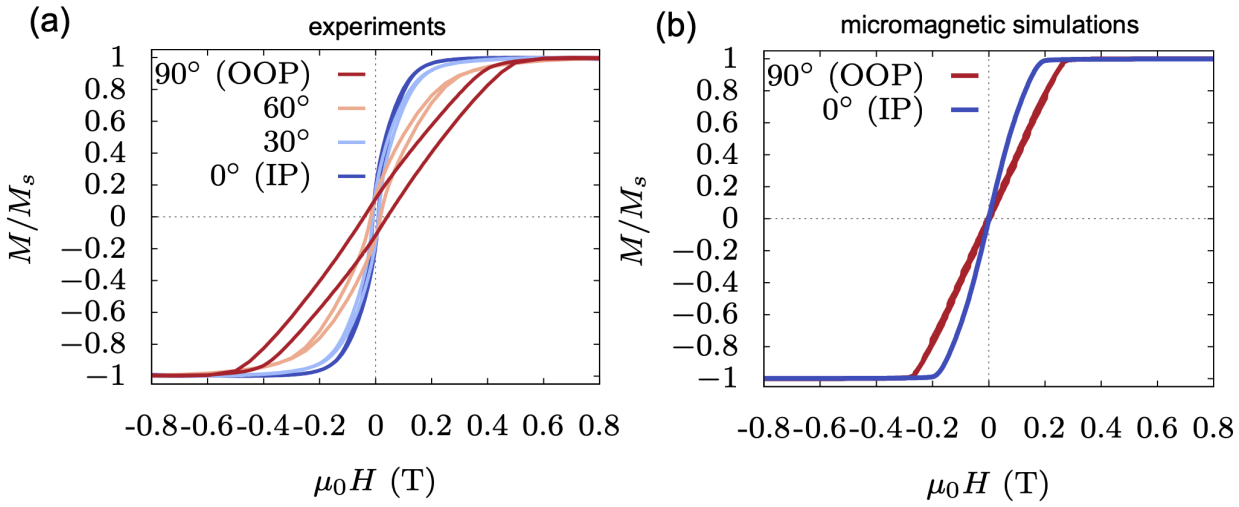

FIG. S7. Angle-dependent hysteresis loops. (a) Experimental data and (b) micromagnetic simulations.

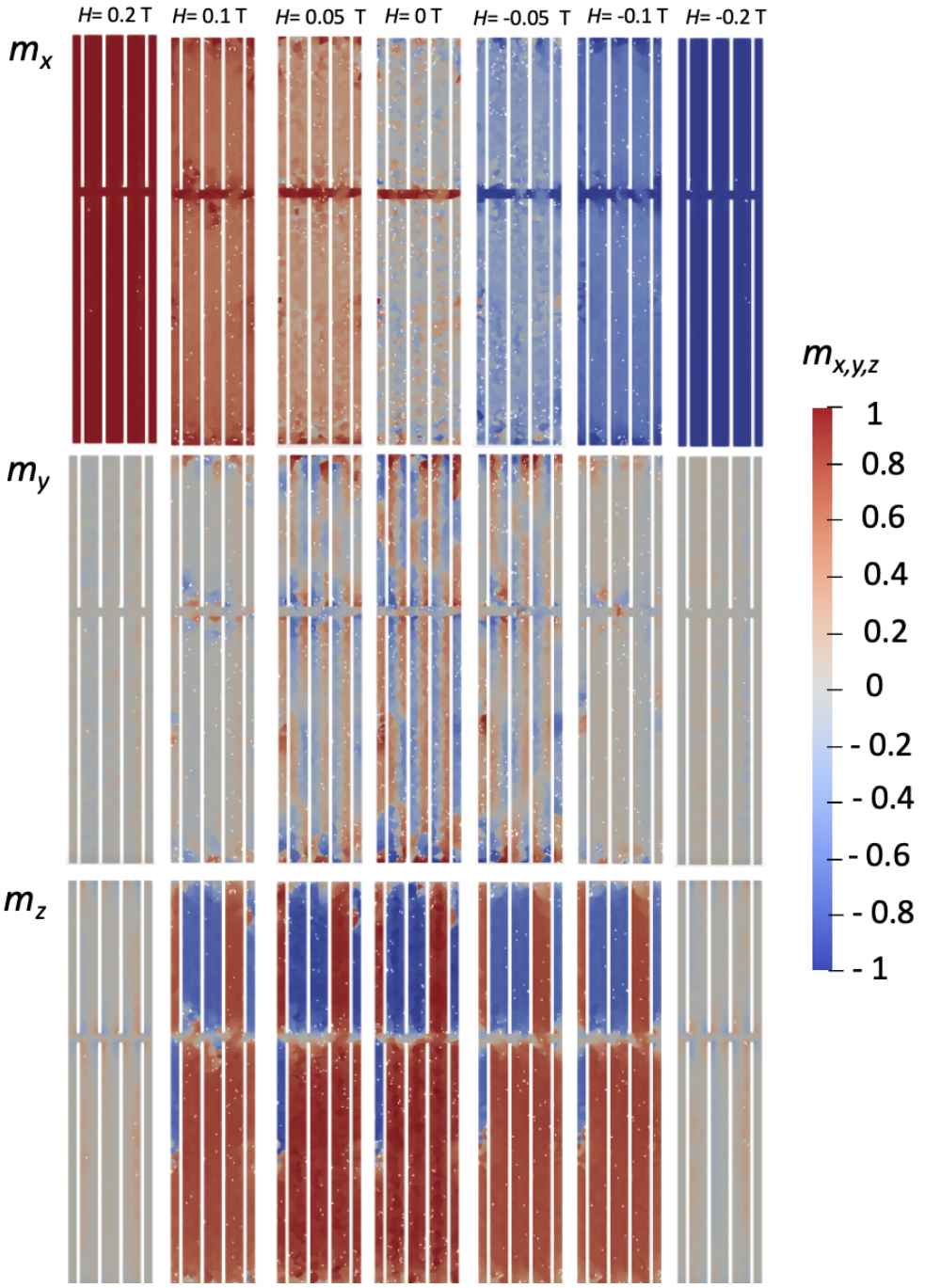

FIG. S8. Magnetic configurations during reversal for the IP configurations of a slice of the central nanowires in our micromagnetic model at various magnetic field strengths around remanence. (Top panel) Micromagnetic configurations of the m_x component. (Middle panel) Micromagnetic configurations of the m_y component. (Bottom panel) Micromagnetic configurations of the m_z component.

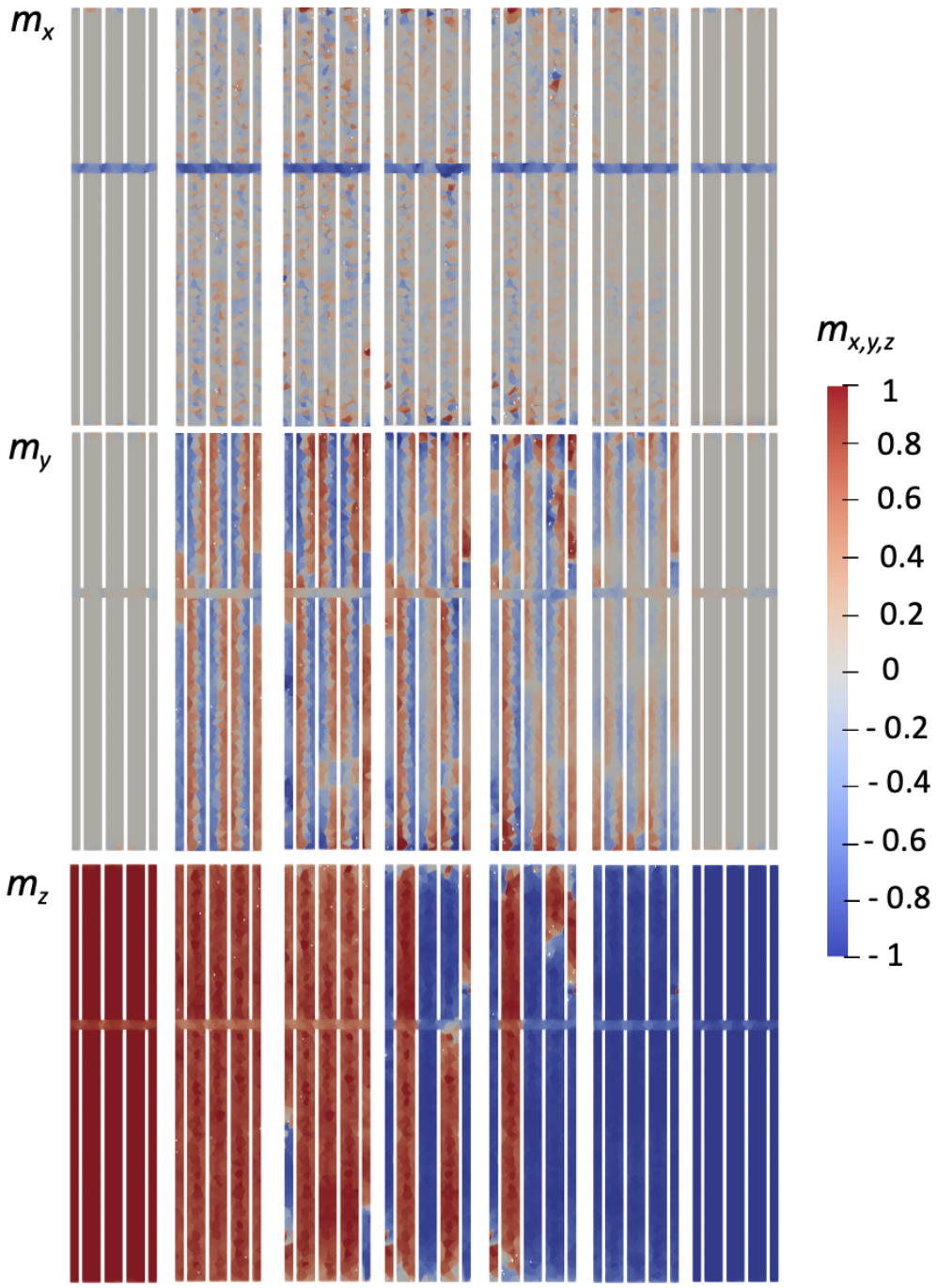

FIG. S9. Magnetic configurations during reversal for the OOP configurations of a slice of the central nanowires in our micromagnetic model at various magnetic field strengths around remanence. (Top panel) Micromagnetic configurations of the m_x component. (Middle panel) Micromagnetic configurations of the m_y component. (Bottom panel) Micromagnetic configurations of the m_z component.

S6. Magnetization reversal mode dependence on the randomly distributed in-plane magnetoelastic anisotropy value

We conducted additional computer simulations varying the magneto-elastic anisotropy from 0 to 5×10^4 J/m^3, as shown in Fig. S10. The results reveal that delocalized reversal dominates up to relatively large values of $K_{\mathrm{me}} = 1 \times 10^4$ J/m^3. As K_{me} increases beyond this threshold, localized reversal begins to emerge.

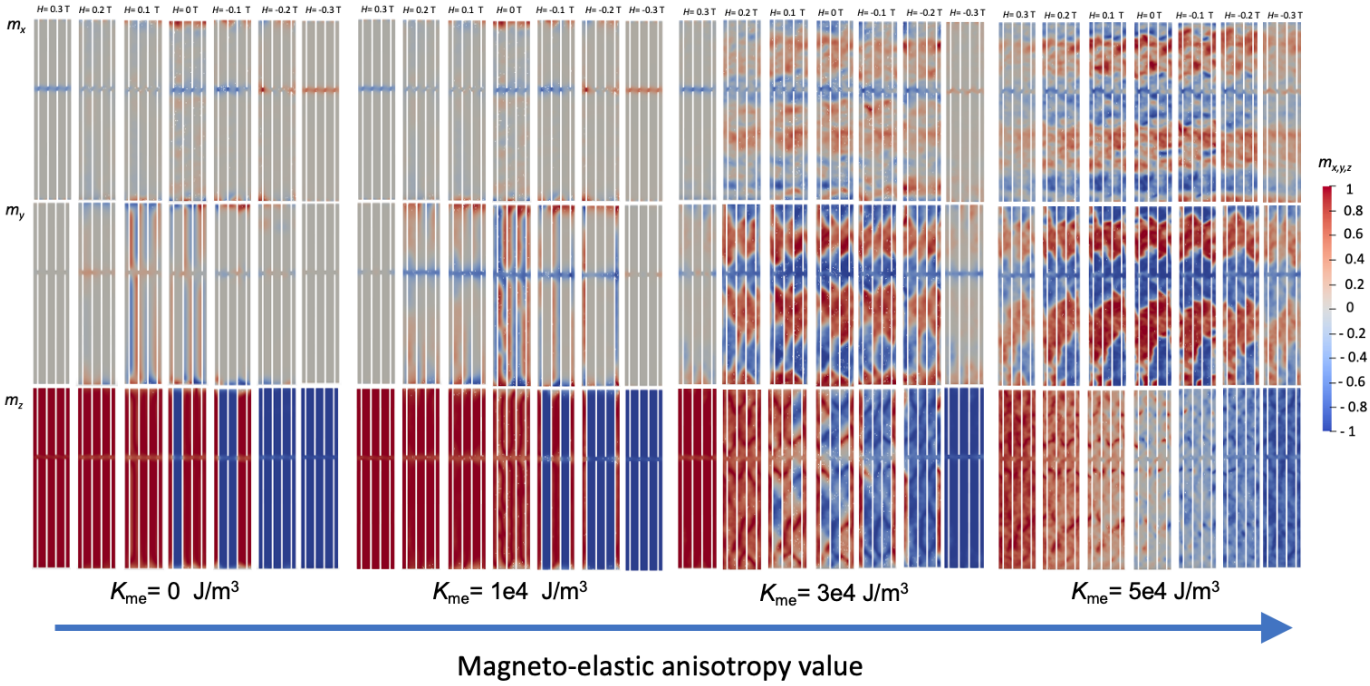

FIG. S10. Magnetization reversal modes dependence on the value of the random in-plane magnetoelastic anisotropy. Magnetic configurations during reversal for the OOP configuration of a slice of the central nanowires in our micromagnetic model at various magnetic field strengths around remanence.

S7. Hysteresis loops as a function of temperature

We have measured and computed hysteresis loops as a function of temperature for the OOP configuration shown in Fig. S11.

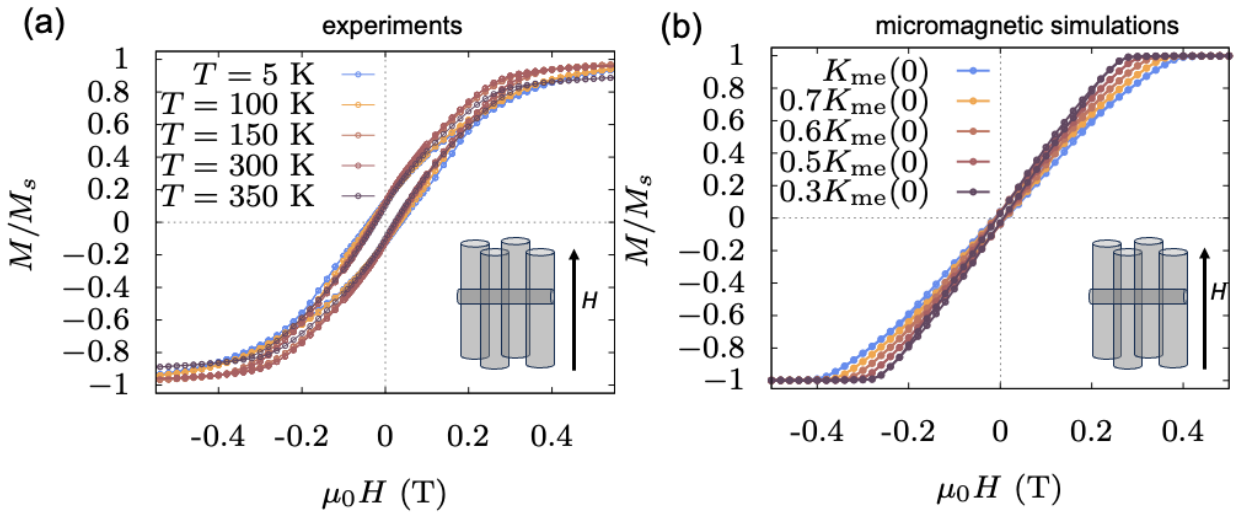

FIG. S11. Hysteresis loops as a function of temperature for the OOP configuration. (a) Experimental data, with temperatures ranging from $T = 5$ K to 350 K. (b) Micromagnetic simulations with anisotropy values scaled relative to $K_{me}(T = 0)$, mimicking the effect of temperature.

As the temperature decreases, the in-plane character of the magnetic response strengthens, the effective in-plane anisotropy increases. Compare the IP and OOP hysteresis loops as a function of temperature in Fig. S12.

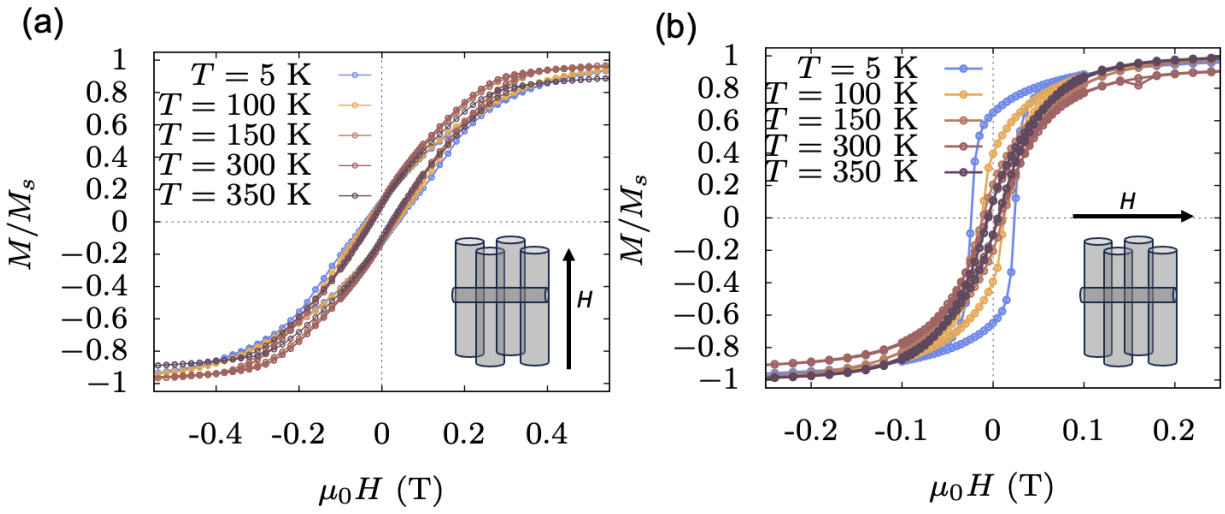

FIG. S12. Temperature dependente hysteresis loops for (a) OOP configuration (external field parallel to the axial direction) and (b) IP configuration (external field perpendicular ot the axial direction).

S8. Magnetic configurations during reversal for the IP configuration around remanence for low temperature

Figure S13 shows the microscopic view of the reversal mechanism for the low-temperature case, $K_{\mathrm{me}}(0)$. It can be observed that the first jump corresponds to $H = -0.02$ T, when a large transverse domain spanning different nanowires is created. The second jump corresponds to a similar process occurring around $H = -0.035$ T. These results suggest that the reversal starts to delocalize; however, instead of occurring along the axial direction of the individual nanowires, it proceeds across the transverse direction. This behavior aligns with the dominating in-plane magneto-elastic anisotropy.

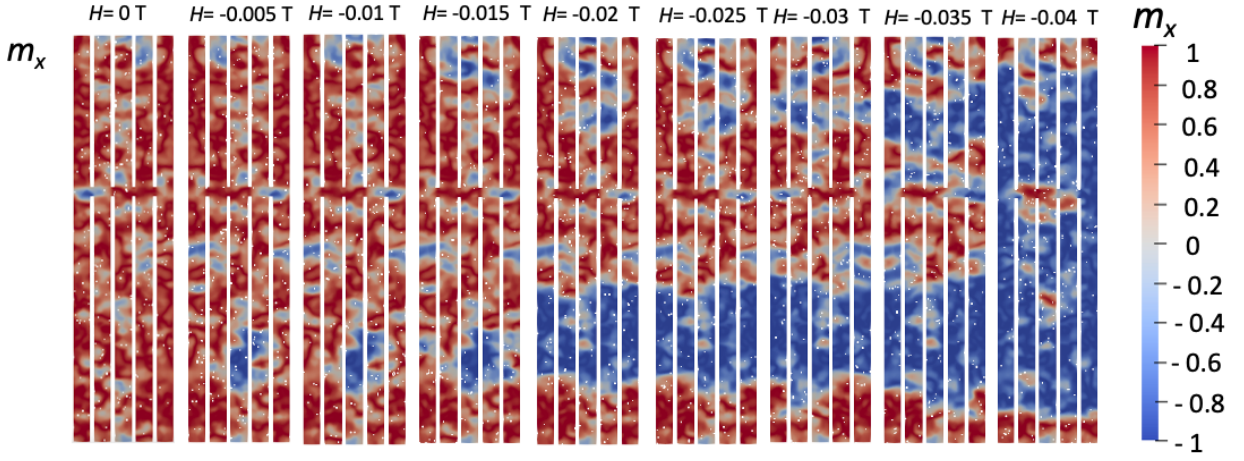

FIG. S13. Magnetic configurations during reversal for the IP configuration of a slice of the central nanowires in our micromagnetic model at various magnetic field strengths around remanence corresponding to the jumps in the hysteresis loop of the Fig. 8 b in the main text, case $K_{\mathrm{me}}(0)$.

S9. Hysteresis loops as a function of the number of nanowires

We have conducted micromagnetic simulations of hysteresis loops for a range of nanowire numbers, $N = 7, 13, 19, 23$. See Figs. S14(a) and (b) for the IP and OOP configurations, respectively. We find that the results depend on the number of nanowires considered, but they already converge for $N = 23$.

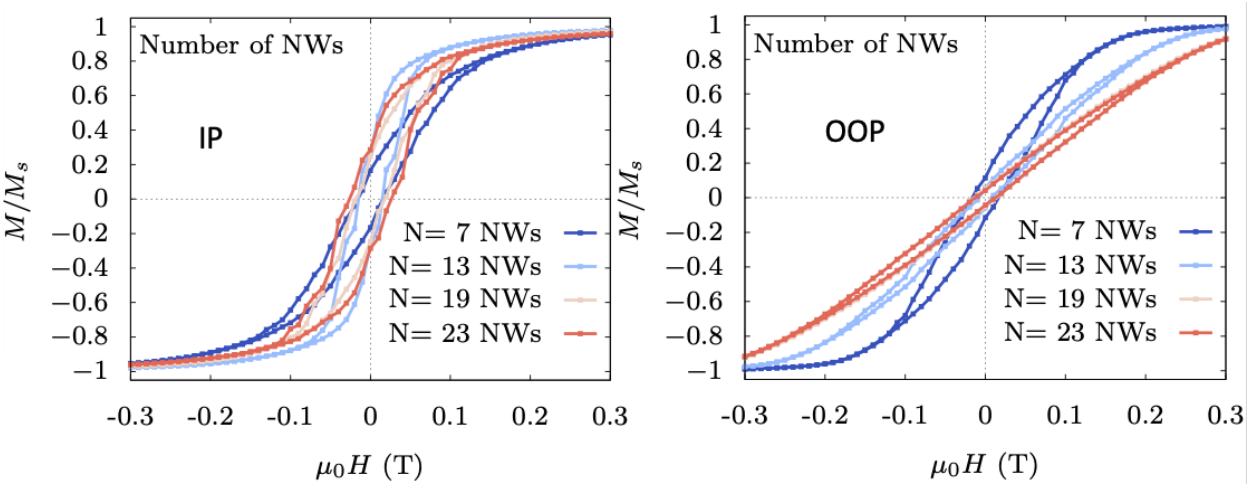

FIG. S14. Hysteresis loops calculated via micromagnetic simulations for a range of nanowire number N. (a) In-plane (IP) configuration. (b) Out-of-plane (OOP) configuration.

REFERENCES

[1]E. A. Marquis, *Microscopy and Microanalysis*, 2005, **11**, 1684–1685.